Electrochemical Activation of Li_2MnO_3 Electrodes at 0 °C and Its Impact on the Subsequent Performance at Higher Temperatures

Francis Amalraj Susai[a], Michael Talianker[b], Jing Liu[c], Rosy[a], Tanmoy Paul[d], Yehudit Grinblat[a], Evan Erickson[az], Malachi Noked[a], Larisa Burstein[e], Anatoly I. Frenkel[f], Yoed Tsur[g], Boris Markovsky[a*z], Doron Aurbach[a**]

[a]*Department of Chemistry and Institute of Nanotechnology and Advanced Materials, Bar-Ilan University, Ramat-Gan 52900, Israel*

[b]*Department of Materials Engineering, Ben-Gurion University of the Negev, Beer-Sheva 84105, Israel*

[c]*Department of Physics, Manhattan College, Riverdale, New York 10471, United States*

[d]*Institute of Physics, Academia Sinica, Taipei, Taiwan, 11529*

[e]*The Wolfson Applied Materials Research Centre, Tel-Aviv University, Tel-Aviv 69978, Israel*

[f]*Department of Materials Science and Chemical Engineering, Stony Brook University, Stony Brook, New York 11794, United States*

[g]*Department of Chemical Engineering and the Grand Technion Energy Program, Technion-Israel Institute of Technology, Haifa 3200003, Israel*

Keywords: lithium-ion batteries; Li and Mn-rich materials; Li_2MnO_3 activation at 0 °C; stabilized cycling; decreased the voltage hysteresis; layered-to-spinel transition; bulk/surface characteristics.

Abstract (200 words)

This work continues our systematic studies of Li and Mn-rich cathodes for lithium-ion batteries. We have chosen Li_2MnO_3 as a model electrode material aiming to correlate improved electrochemical characteristics of these cathodes initially activated at 0°C with structural evolution of Li_2MnO_3, oxygen loss, formation of per-oxo like species $(O_2)^{n-}$, and the surface chemistry. It was established that performing a few initial charge/discharge (activation) cycles of Li_2MnO_3 at 0°C, resulted in increased discharge capacity, higher capacity retention, decreased and substantially stabilized the voltage hysteresis upon subsequent cycling at 30°C or at 45°C. In contrary to activation of Li_2MnO_3 at these *higher temperatures*, Li_2MnO_3 underwent step-by-step activation at 0°C, providing a few-steps stepwise traversing of the voltage plateau at >4.5 V during initial cycling. Importantly that these findings agree well with our previous studies on activation at 0°C of $0.35Li_2MnO_3 \bullet 0.65Li[Mn_{0.45}Ni_{0.35}Co_{0.20}]O_2$ materials. We proposed stabilized interface is developed at 0°C that can be ascribed to the reduced interactions of the per-oxo like species formed and the oxygen released from Li_2MnO_3 with the solvents in ethylene carbonate – methyl ethyl carbonate/$LiPF_6$ solutions. Our TEM studies revealed that typically, upon initial cycling both at 0°C and at 30°C, Li_2MnO_3 underwent partial structural layered-to-spinel ($Li_2Mn_2O_4$) transition.

1. Introduction

Among various materials for cathodes in advanced Li-ion batteries (LIB), Li and Mn-rich oxides like $Li_{1+x}Ni_yCo_zMn_{0.5+w}O_2$ (x + y + z + w = 0.5) or $xLi_2MnO_3•(1-x)LiMO_2$ (M = Mn, Ni, Co) are the most promising because of their high discharge capacity (> 250 mAh/g) after the first activation charge-discharge cycle and high energy density of ~1000 Wh/kg. These materials have attracted much attention since they were first synthesized and introduced by Thackeray et al. and intensively studied by many groups [1–7]. Electrodes comprising these high-energy lithiated Ni, Co, Mn oxides (HE-NCM) suffer from fast capacity fading, large the voltage hysteresis, and transition metals dissolution during prolonged cycling [5,8–18]. Therefore, researchers have proposed several approaches to stabilize their electrochemical performance, such as surface coatings by oxides and salts, for instance Al_2O_3, TiO_2, ZrO_2, AlF_3 [19–21], cationic or anionic lattice doping with Na^+, Mg^{2+}, Al^{3+}, F^-, etc. [22–26], and gas treatment at high tempature with NH_3, SO_2, CO_2, or F_2 [27–30]. Additionally, Thackeray et al. [31,32] have shown that treatment of HE-NCM materials with inorganic acids (H_2SO_4, HNO_3) resulted in a stable electrochemical behavior. We have demonstrated recently [33] that stable cycling and higher rate capability, lower the voltage hysteresis of HE-NCM cathodes in Li-cells can be achieved after treatment of these materials with trimesic or terephthalic acids at 600 °C. An important finding was reported in our previous work [34] that performing initial (activation) cycling of HE-NCM electrodes at low temperature, for instance 0 °C or 15 °C, resulted in higher discharge capacity, decreased the voltage hysteresis and its stabilization compared to those electrodes initially activated and cycled at the higher temperatures (30 ° and 45 °C). In that work, we used $0.35Li_2MnO_3•0.65Li[Ni_{0.35}Mn_{0.45}Co_{0.20}]O_2$ material reffered as a two-phase system consisting of layered structurally compatible components:

Li_2MnO_3 (monoclinic, space group C2/m) and $Li[Ni_{0.35}Mn_{0.45}Co_{0.20}]O_2$ (rhombohedral, space group R-3m) integrated on a nano-scale [8,11,35–37] and demonstrating common *d*-spacing [38]. Li_2MnO_3 attracts attention not only as one of the end-members of HE-NCM materials, but as a high-capacity cathode with theoretical capacity ~460 mAh/g for total Li extraction when charged to potentials >4.6 V. However, Li_2MnO_3 becomes electrochemically active in electrodes comprising its nano-sized particles which demonstrate higher capacity and enhanced cycling behavior compared to those of submicronic or micron-sized materials. Li_2MnO_3 component plays a critical role in HE-NCM cathodes providing high capacity during cycling in the potential range of 2.0 – 4.6 V by introducing a reversible anionic red-ox chemistry, $O^{2-} \rightarrow (O_2)^{n-}$. This oxygen redox compensates for almost half of the measured capacity of HE-NCMs in the initial cycles, and more than one-third of the capacity is still contributed from reversible oxygen redox after 70 cycles as established recently by Tarascon et al. [38]. In light of numerous experimental [39–45] and theoretical [46–50] studies of Li and Mn-rich layered materials as cathodes in Li-cells, much effort is still required to reveal the relationship among composition of these materials, structure, layered-to-spinel phase transformations, and enhanced electrochemical characteristics depending on cycling conditions (potential window,current density applied), electrolyte solutions, and temperature.

The main goal of the present work, which is a continuation of our recent research [34], was to study how the initial (activation) cycling of Li_2MnO_3 electrodes at low temperature (0 °C) influences their subsequent electrochemical performance at the higher temperatures (for instance, 30 °C and 45 °C). We aimed also to correlate improved electrochemical characteristics of these electrodes - stabililized capacity and the voltage hysteresis - with structural evolution of Li_2MnO_3, oxygen loss, formation of per-oxo like species $(O_2)^{n-}$, and surface chemistry. Thus, we intended to

deeply understand the basic phenomenon of the temperature-dependent activation ("low-T activation") of xLi_2MnO_3•$(1-x)Li[Ni\text{-}Mn\text{-}Co]O_2$ materials at 0 °C, studied for the first time.

2. Materials and Methods

2.1 Synthesis of Li_2MnO_3

Li_2MnO_3 was produced by the solution-combustion reaction (SCR) from an aqueous solution of lithium nitrate LiOH and manganese nitrate $Mn(NO_3)_2$ (Sigma-Aldrich), which act as the oxidants, and sucrose $C_{12}H_{22}O_{11}$ as the fuel, similarly to the previous reports [51]. The oxidant/fuel ratio was 1:1. The as-prepared Li_2MnO_3 material was annealed at 400 °C and 700 °C for 1 h in air at each temperature. The individual primary particles obtained were of 30-100 nm, some of which were agglomerates of ~1 – 1.5 μ. The SEM image is presented in **Figure S1.** The specific active surface area was ~20 $m^2\ g^{-1}$ as measured by Brunauer, Emmet and Teller (BET) method (Gemini 2375, Micromeritics, multipoint mode). The chemical analysis of the annealed product was carried out using the inductive coupled plasma technique (ICP-AES, spectrometer Ultima-2 from Jobin-Yvon Horiba). The composition of the material was Mn:Li=1:2 corresponding to Li_2MnO_3 within the accuracy of the measurement ~98%.

2.2 Preparation of electrodes and electrochemical cells

Working electrodes (cathodes) for electrochemical cells were prepared by mixing the active material Li_2MnO_3 with carbon black super P (from Timcal), graphite KS-6 (Timcal) and polyvinylidene difluoride binder PVdF (Solef 5130) in a ratio of 80:10:10 wt.%, in N-methyl pyrrolidone using planetary vacuum mixer Thinky (Japan) to obtain slurry. It was then cast onto

an aluminum foil (15 μm thick, from Strem), dried on a hotplate followed by drying at 120 °C under vacuum overnight.

2.3 Electrochemical measurements

Electrochemical tests were carried out in two-electrode cells of 2325 coin-type configuration. The geometric area of the working electrodes was ~1.5 cm^2 and the average loading of the active mass was ~3 mg/cm^2. Counter electrodes were prepared from ~200 μm thick lithium foil. Electrochemical cells were assembled in a glove box (VAC) filled with highly pure argon (5N). The electrolyte solutions (Li battery grade, LP57 from BASF) comprised 1M $LiPF_6$ dissolved in ethyl-methyl carbonate (EMC) and ethylene carbonate (EC), weight ratio 7:3. For statistical purposes, we studied electrochemical perfromance of at least 2 – 3 cells simultaneously and the results were averaged. The electrochemical measurements were performed using a multichannel Maccor-2000 battery cycler and a battery test unit model 1470, coupled with a FRA model 1255 from Solartron, Inc. (driven by Corrware and ZPlot software from Scribner Associates, Inc.). The alternating voltage amplitude in impedance measurements was 3 mV and the frequency ranged from 100 kHz to 5 mHz. The electrochemical impedance spectroscopy data were analyzed using Impedance Spectroscopy Genetic Programing (ISGP), a matlab based program that finds the distribution function of relaxation times (DFRT) via genetic programming [52–54]. ISGP finds an analytical form of the DFRT, which makes it possible to follow the changes in each peak that idealy represents a process. All the potentials in this paper are given *vs.* Li^+/Li. Electrochemical tests and on-line electrochemical mass spectrometry measurements were conducted in thermostats at 0 °C (from Binder) and higher temperatures (from MRC).

2.4 Structural and surface studies

X-ray powder diffraction (XRD) measurements were performed in the 2θ range from 10 to 80°, with a step size of 0.02° at 15 sec/step rate. The analysis of the XRD patterns was carried out using the PowderCell program [55] and the Fullprof program as described elsewhere [56]. Transmission electron microscopy (TEM) studies of the Li_2MnO_3 particles were performed with a LaB_6-200 kV Jeol-2100 electron microscope and convergent beam electron diffractions (CBED) were taken using a 7 nm probe size. Samples for the TEM studies were prepared by methodology described in ref. [57]. Scanning electron microscopy (SEM) images of Li_2MnO_3 powder were obtained using E-SEM (environmental scanning electron microscope), Quanta FEG. Micro-Raman spectroscopy measurements of electrodes and powders scratched from them were performed at room temperature using a micro-Raman spectrometer from Renishaw inVia (United Kingdom) equipped with a 514 nm laser, a CCD camera, and an optical Leica microscope. A 50x objective lens to focus the incident beam and an 1800 lines/mm grating were used. For statistical purposes, Raman spectra were recorded from 10–20 locations arbitrarily chosen on a sample. X-ray Photoelectron Spectroscopy (XPS) measurements were performed in ultrahigh vacuum ($2.5x10^{-10}$ Torr base pressure) using a 5600 Multi-Technique System (PHI, USA). The samples were irradiated with an Al Kα monochromated source (1486.6 eV) and the outcome electrons were analyzed by a spherical capacitance analyzer using the slit aperture of 0.8 mm in diameter. High resolution spectra were taken at pass energy of 11.75 eV at increments of 0.05 eV/step to allow precise energy position and peak shape determination. Curve fitting was done with a Gaussian-Lorentzian function using the 5600 Multi-Technique System software. Mn K-edge X-ray absorption fine structure (XAFS) spectroscopic measurements of Li_2MnO_3 were carried out at BL2-2 beamline at Stanford Synchrotron Radiation Light source (SSRL) in transmission mode. The Li_2MnO_3 sample was ground to fine powder and brushed on tape for measurements. XAFS data processing and analysis

were done using the Athena and Artemis software within the IFEFFIT package [58]. The normalized k^2-weighted EXAFS data were Fourier transformed in a k range of 2-11 $Å^{-1}$ for Mn. In the fits, the contributions from two metal−oxygen (M−O) paths with different interatomic distance and one metal−metal (M−M) path according to the Li_2MnO_3 structure were included. The value of the amplitude reduction factor (S_0^2) was obtained from the fitting of the pristine Li_2MnO_3 powder and fixed in the fits of the electrode materials.

2.5 On-line electrochemical mass spectrometry

A customized on-line electrochemical mass spectrometer (OEMS) with multi-inlet capillary system (Hiden Analytical) was used to analyze the evolving gases, in-operando, as a function of the applied potential and temperature. A laboratory-made cell for the OEMS measurement were assembled inside Ar filled glovebox with Li_2MnO_3 as cathode (ø 10 mm), Li foil as anode (ø 14 mm), and 100 µL LP 57 as electrolyte solution. Two polyethylene separators (ø 29 mm) were placed between cathode and anode. The cell was connected to OEMS through a microcapillary using one of the Swagelok valves located at the head part of the cell. A vacuum of 10^{-6} torr was maintained while sampling the evolved gases at a rate of 12 µL/s. The electrochemical measurements were carried out using VSP-potentiostat (Bio-logic Science instruments) in a potential window of 2.4– 4.7 V. The variation of desired gases with time was investigated using Mid mode. The measurements were carried out at 0 and 30 ˚C using thermostats.

3. Results and Discussion

3.1 Structural and morphological characteristics of Li_2MnO_3

Figures S1 and **S2**, respectively, represent the SEM image of the Li_2MnO_3 particles measured from the as-prepared annealed product and its XRD profile. It can be seen in **Figure S1** that the shape of primary particles is almost equiaxed of about 30 – 100 nm in size, some of which form submicronic and micron-sized aggregates. The XRD pattern in **Figure S2** shows peak positions characteristic of the Li_2MnO_3 phase that correspond to the *C2/m* symmetry including weak overlapping peaks (020) and (110) at 2ϑ=20 - 22^0, which arise due to ordering in the transition metal layers comprising Li and Mn ions in an atomic ratio 1:2. This is in accordance with the approach describing the monoclinic Li_2MnO_3 structure [59,60] as a layered compound similar to $LiMO_2$, thus representing the formula Li_2MnO_3 in layered notation as $Li[Li_{1/3}Mn_{2/3}]O_2$ while the ordered $[Li_{1/3}Mn_{2/3}]$ layers are stacked along the *c*-axis.

The unit cell parameters of the monoclinic phase as calculated from the XRD data (reliability factor of R_p=2.55%) are as follows: a=4.926 Å, b =8.512 Å, c =5.022 Å, β=109.33^0, which is in line with the values reported in the literature [60].

The results of TEM analysis are consistent with the structural information obtained by XRD. The TEM image of individual particles of the annealed as-synthesized material is represented in **Figure 1** with an insert showing the CBED pattern, which was taken from the particle indicated by the arrow and indexed on the basis of the monoclinic Li_2MnO_3 structure. Small region of this particle was also used to obtain a high-resolution image shown in **Figure S3.** As expected, the distances measured between the atomic planes were 0.43 nm and 0.41 nm, thus matching, respectively, the interplanar spacings d_{020} and d_{110} in the monoclinic Li_2MnO_3 structure. Furthermore, Fourier

transform (see insert) of a part of the image looks exactly the same as the CBED pattern (**Figure 1**) recorded in the diffraction experiment.

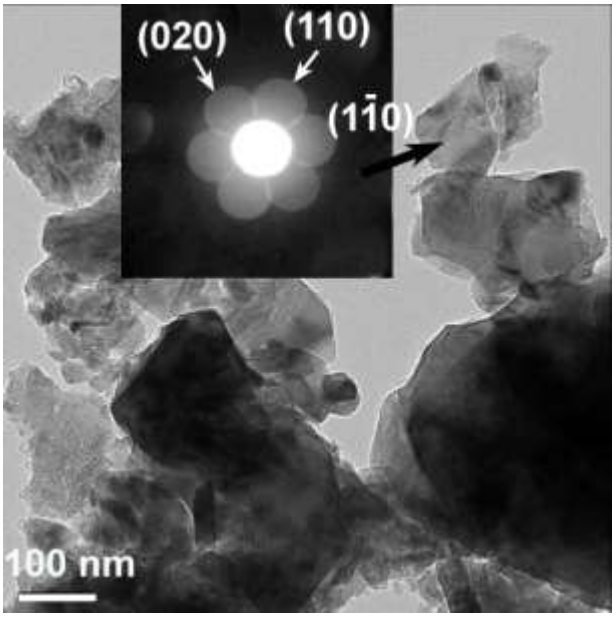

Figure 1. Bright field TEM image of the particles of pristine Li_2MnO_3 material. The insert shows an example of CBED pattern, which was taken from the particle indicated by arrow. The pattern was indexed on the basis of the monoclinic Li_2MnO_3 structure.

3.2 Electrochemical behavior and structural evolution of Li_2MnO_3 electrodes at 0 ℃, 30 ℃, and 45 ℃. Impact of their initial activation cycling at 0 ℃.

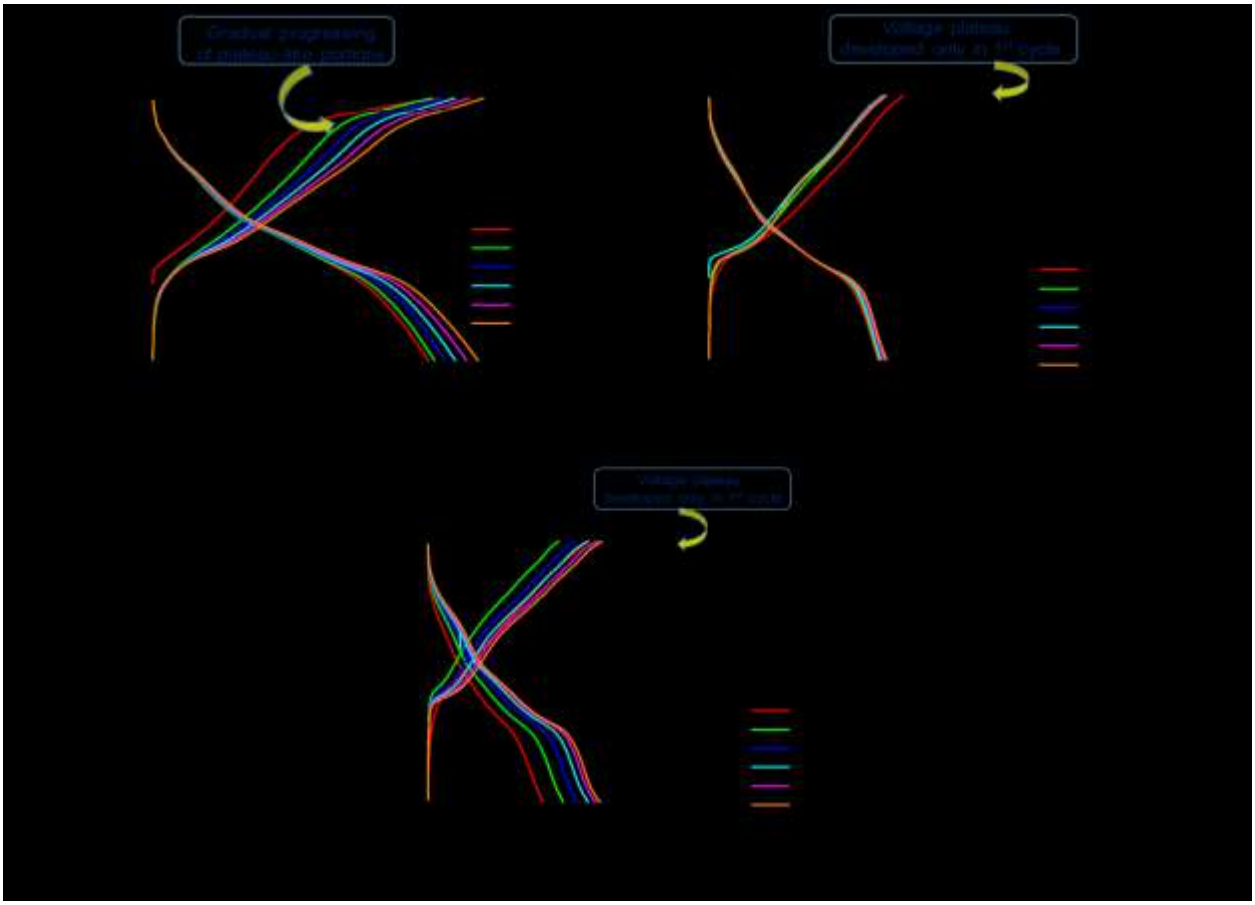

Figure 2a, b, c. Voltage profiles of Li_2MnO_3 electrodes measured during several initial cycles at 0 °C ***(a)***, 30 °C ***(b)***, and 45 °C ***(c)***. The current density applied was 2 mA/g. Potentials of the plateaus registered upon the charging of electrodes to 4.7 V are indicated. At the upper cut-off voltage of 4.7 V, electrodes were kept potentiostatically for 1 hour. Note that at 0 °C, plateau-like portions of the charging profiles registered at ~4.55 V are developed in a step-wise manner, as indicated in ***(a)***.

In **Figure 2a, b** and **c**, we compare the voltage profiles measured during the initial charge-discharge cycles from Li_2MnO_3 electrodes at 0 °C, 30 °C and 45 °C, respectively. The first charging processes for all of these electrodes up to 4.7 V are characterized by a steep potential increase in the potential range from OCV to ~4.4 - 4.5 V, at which Li_2MnO_3 is electrochemically inactive, followed by an irreversible potential plateau related to the Li_2MnO_3 activation and the Li^+ deintercalation, in agreement with the literature reports [41,42]. Importantly to note that upon the initial charge reaction, the potential plateaus were registered at 4.66 V, 4.60 V, and 4.55 V for the above Li_2MnO_3 electrodes at 0 °C, 30 °C, and 45 °C, respectively. This observation is in line with our finding in a previous study [34], in which Li_2MnO_3-based Li and Mn-rich electrodes $0.35Li_2MnO_3{\cdot}Li[Mn_{0.45}Ni_{0.35}Co_{0.20}]O_2$ at 0 °C exhibited the 1st charging voltage plateau at ~4.7 V that was 150 – 200 mV higher comparing to those measured at 15 °C, 30 °C, and 45 °C. In addition, only at 0 °C, charge profiles exhibit short plateau-like portions at around 4.50 – 4.55 V formed continuously during charging to 4.7 V in 2nd to 5th cycles. This continuously developed plateau-like portions of the charging process at 0 °C, though at lower potentials compared to the plateau during the first charge (**Figure 2a)**, seems to be thermodynamically favorable and may indicate a continuous activation of Li_2MnO_3 and the Li^+ extraction from the structure. They are gradually progressing, in contrast to the voltage plateaus that were developed only in the first charging process of Li_2MnO_3 electrodes at 30 °C and 45 °C shown in **Figure 2b** and **c**. In addition, **Figure S4** that shows differential capacity plots of the above Li_2MnO_3 electrode cycled at 0 °C, also exhibits dQ/dV peaks at potentials close to those of the voltage plateaus.

A similar continuous activation of Li_2MnO_3 reflected by gradually developed plateau-like portions during charging to 4.8 V for the initial five cycles was also established by Ye et al. [61] in Li-rich $Li[Li_{1/3-2x/3}Mn_{2/3-x/3}Ni_x]O_2$ ($0.09 \leq x \leq 0.2$) materials doped with minor amount of Nickel. These authors attributed the continuous or stepwise gradual activation of Li_2MnO_3 as promoted by smaller (optimized) amounts of the dopant.

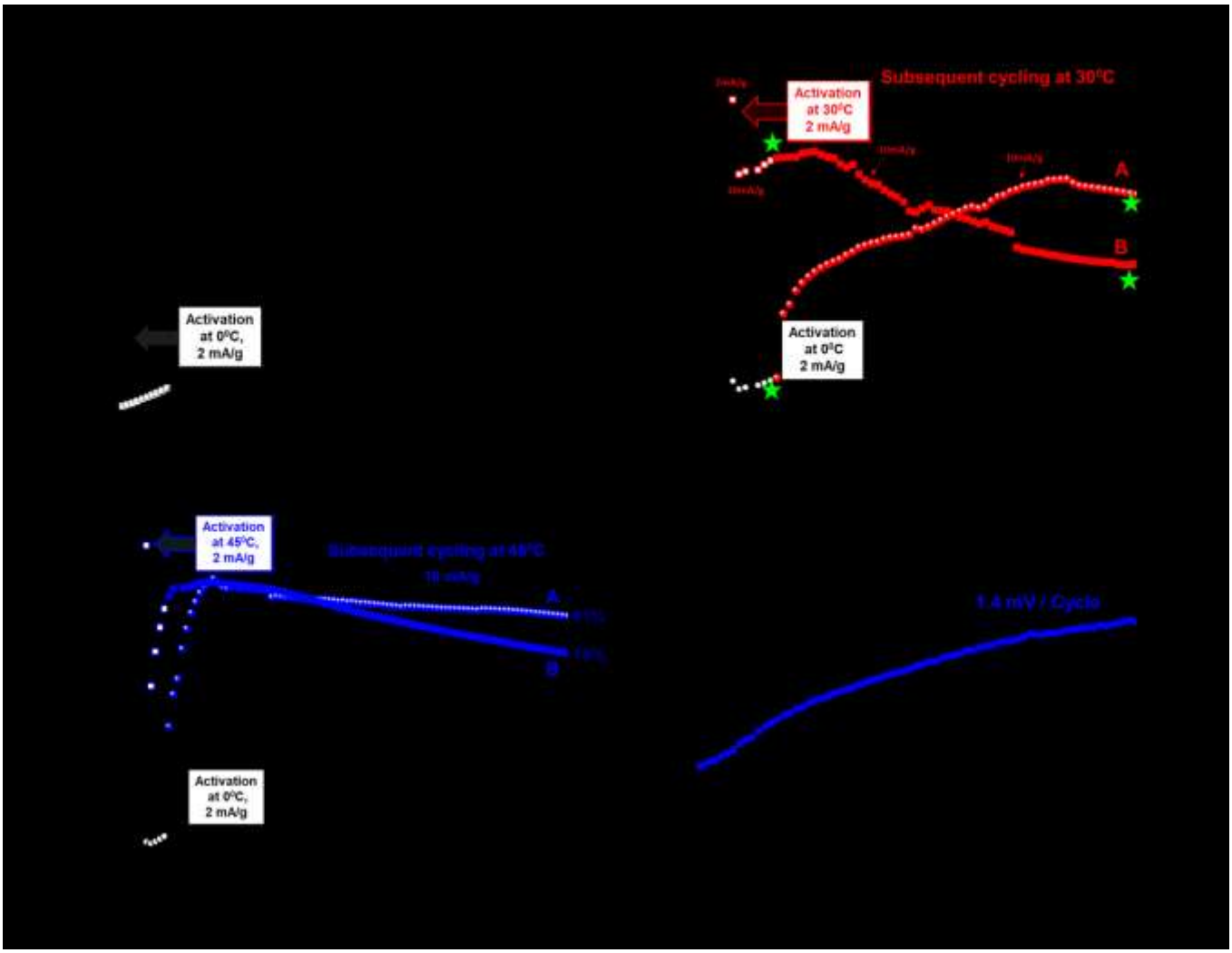

Figure 3. (a) Discharge capacity of Li_2MnO_3 electrodes activated at 0 °C for several initial cycles (empty symbols). Current density was 2 mA/g corresponded to ~C/10 rate. Subsequent cycles (10

mA/g, ~C/2 rate) at this temperature is also shown (filled symbols). (b) Left hand portion: discharge capacity of several initial activation cycles of Li_2MnO_3 electrodes at 0 °C (black symbols; 2 mA/g, ~C/10) and at 30 °C (red symbols). In the right hand portion, curve **A** exhibits discharge capacity of Li_2MnO_3 electrodes activated at 0 °C and subsequently cycled at 30 °C (10 mA/g, ~C/2). Curve **B** relates to the case when both activation and the subsequent cycling were performed at 30 °C. Note that in both cases of activation at 0 °C or at 30 °C, the subsequent cycling was performed at the same C/2 rate, for the direct comparison. Impedance spectra of Li_2MnO_3 electrodes were measured at 30°C, at 4.4 V upon charging at points marked with green stars. Typical impedance spectra are shown in **Figure S5**. (c) Left hand portion: discharge capacity of several initial activation cycles of Li_2MnO_3 electrodes at 0 °C (black circles; 2 mA/g, ~C/10) and 45 °C (blue squares). In the right hand portion, curve **A** exhibits discharge capacity of Li_2MnO_3 electrodes activated at 0 °C and subsequently cycled at 45 °C (10 mA/g, ~C/2). Curve **B** relates to the case when both activation and the subsequent cycling were performed at 45 °C. Capacity retention (in %) of these electrodes calculated from 20^{th} to 95^{th} cycles is indicated. (d) Black curve displays the voltage hysteresis of Li_2MnO_3 electrodes activated at 0 °C for a few initial cycles and subsequently cycled at 45 °C. Blue curve: both activation and the subsequent cycling were performed at 45 °C, as demonstrated in **Figure 3c.** Changes of the voltage hysteresis per cycle are indicated.

Figure 3a, b, and **c** shows that the discharge capacities delivered in the initial cycles at 0 °C and 45 °C increased up to ~22 and 100 mAh/g respectively, while those at 30 °C were stabilized at

around 90 mAh/g. We note that the relatively low capacities obtained at 30 °C and 45 °C from electrodes comprising Li_2MnO_3 submicronic (partially agglomerated) particles are in line with those values demonstrated in our previous work [51]. The complex process of the Li^+-ions extraction above 4.5 V from Li and Mn-rich electrodes involves the potential plateau, the simultaneous oxygen extraction from the lattice, and rearrangement of Mn-ions in case of Li_2MnO_3 or TM-ions (Mn, Ni, Co) in case of $xLi_2MnO_3{\cdot}(1\text{-}x)Li(TM)O_2$ materials. This process can be represented as follows [49, 63]:

$$Li_2MnO_3 \rightarrow 2\ Li^+ + 2e^- + MnO_2 + 1/2\ O_2\uparrow \quad (1)$$

Recent studies by the Gasteiger's group using OEMS and HR-TEM [6,62,63] provided strong evidence that oxygen is released not from the bulk Li_2MnO_3 but irreversibly from a several nm thick near-surface layer of $xLi_2MnO_3{\cdot}(1\text{-}x)Li(TM)O_2$ materials. Importantly to emphasize that upon charging to high potentials oxygen can be oxidized to per-oxo species ($O^{2-} \leftrightarrow O_2^{2-}$) and then released as gas O_2 [38,64]. This reversible oxo- (O^{2-}) to per-oxo like $(O_2)^{n-}$ transformation upon charge/discharge of Li-rich oxides is driven by a reductive coupling mechanism and is still under intensive studies [65,66]. As it follows from the results in **Figure 3a, b,** and **c**, the maximal charge capacities obtained in the 1st cycle at 0 °C, 30 °C, and 45 °C were, respectively 27, 212, and 227 mAh/g. They correspond to ~6, 46, and 49 % of the Li-ions extracted from Li_2MnO_3 taking into account its theoretical capacity of ~460 mAh/g for 2 Li^+ extracted per chemical formula. The corresponding discharge capacities delivered in the 1st cycles at these temperatures were 21, 110 and 113 mAh/g with the calculated irreversible capacity losses (ICL) of 1.8, 51, and 52 % respectively. The lowest ICL at 0 °C implies thus much lesser undesirable side reactions of the

electrode material with traces of HF, PF_5 (strong Lewis acid) in EC-EMC/$LiPF_6$ solution, for instance:

$$Li_2MnO_3\ (s) + PF_5\ (sol) \rightarrow 2\ LiF\ (s) + POF_3\ (gas) + MnO_2\ (s) \quad (2)$$

This may also relate to the reduced interactions of the per-oxo like species formed and the oxygen released at 0 °C with the EC and EMC solvents. $(O_2)^{n-}$ can promote reactions of the EC absorbed on the electrode surface and its decomposition (by breaking one of the two C – O bonds in the ring) that results in evolution of CO_2 and other organic species [67]. Our suggestion on minor interfacial side reactions at 0 °C is consistent with the observed reduced oxygen activity upon charging process at this temperature compared to that at 30 °C. This is demonstrated by the results of OEMS studies in **Figure 4** and agrees well with the surface analysis of the oxygen XPS spectra of Li_2MnO_3 samples subjected to initial cycling at 0 °C and 30 °C.

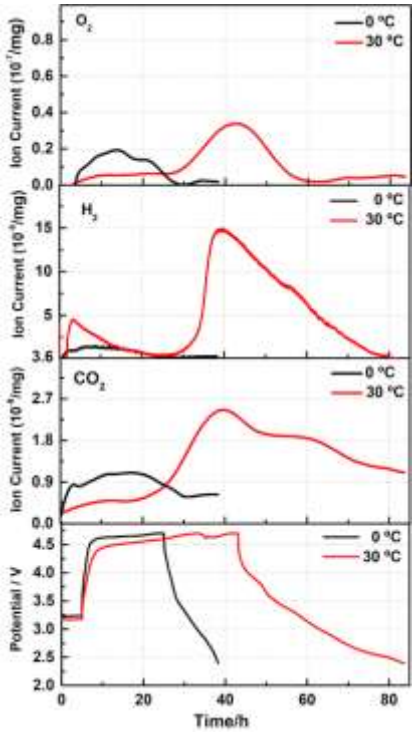

Figure 4. Evolution of gases O_2, H_2, and CO_2 with time during the 1st charge-discharge cycle of Li_2MnO_3 electrodes (shown in the bottom chart) measured by OEMS at 0 °C and 30 °C, as indicated. Since during 2nd to 7th initial cycles much less gases were evolved compared to the 1st one, the corresponding ion currents could be hardly measured because of the instrumental limitations of OEMS. The upper cut-off voltage was 4.7 V in these experiments.

From XPS measurements, we established lower amount (5.2%) of per-oxo like species formed upon the 1st cycle of Li_2MnO_3 electrode at 0 °C compared to that of 11.6% at 30 °C, **Figure 5** and **Table S2**. This is also evident from the comparative ratio of [lattice oxygen] to [per-oxo species], which is almost twice as higher for the latter electrode. Note that the content of $(O_2)^{n-}$ species calculated from our high-resolution XPS studies agrees well with that number of 9% measured for discharged Li-rich $Li_{1.2}Ni_{0.13}Mn_{0.54}Co_{0.13}O_2$ materials presented in the work by Tarascon et al. [38]. We suggest that stabilized Li_2MnO_3 electrode/solution interface is formed during the activation cycles at 0 °C compared to that at 30 °C and 45 °C providing thus their stable subsequent cycling performance with higher capacity retention demonstrated in **Figure 3b** and **c.**

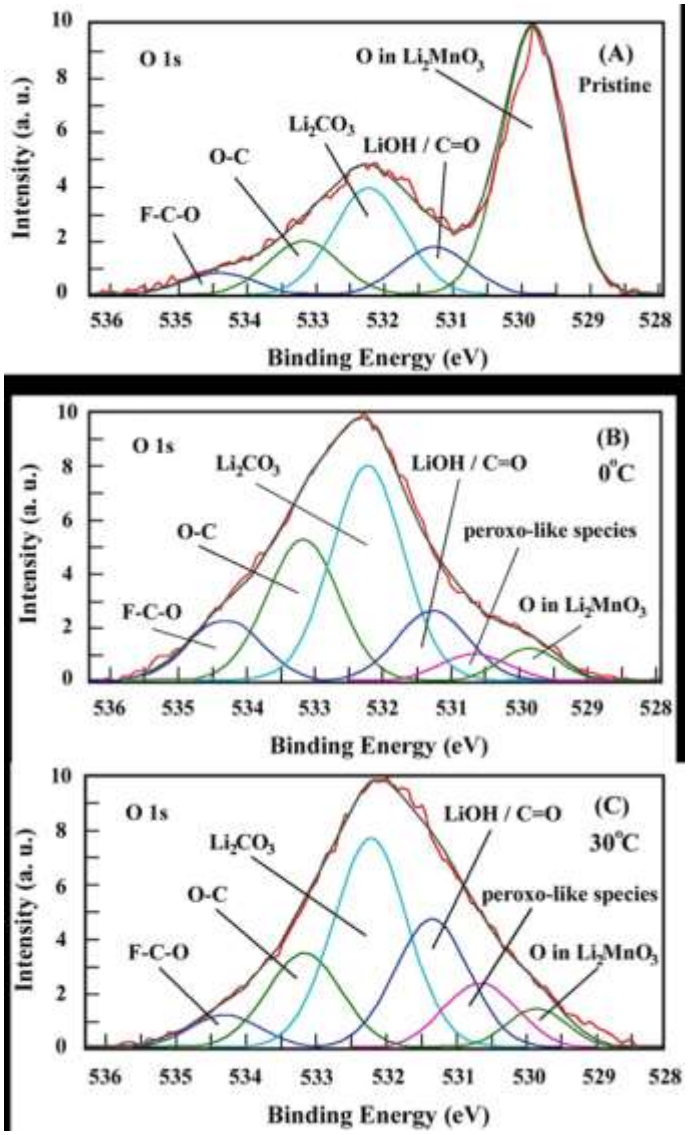

Figure 5. O1s XPS spectra measured from pristine (uncycled) Li_2MnO_3 electrode (A) and those subjected to the 1st charge-discharge cycles at 0 °C and 30 °C, (B) and (C), respectively. Voltage profiles of these electrodes are shown in **Figure 2a** and **b.**

A clear evidence to support our suggestion is a much lower charge-transfer resistance (R_{ct}) of Li_2MnO_3 electrodes initially activated at 0 °C, compared to that of 30 °C, as demonstrated in

Figure 6a. It represents the surface film (R_{sf}) and charge-transfer resistances of these electrodes as a function of the potential measured during charging process up to 4.7 V. **Figure 6b** shows that after 65 cycles, R_{ct} also remains lower for those electrodes activated at 0 °C. Only at 4.6 V, R_{ct} increases, probably due to some structural disordering or rearrangements at the electrode surface at high anodic potentials. Note that information of resistances representing the electrochemical processes (as in **Figures 6a** and **b**) was obtained from the analysis the data in Impedance Spectroscopy Genetic Programing that computes distribution function of relaxation times Γ in the form of Γ plotted vs. log f (f is the frequency ranged from 100 kHz to 5 mHz used in impedance tests). These plots are shown in the Supporting Information, **Figures S5a –d.**

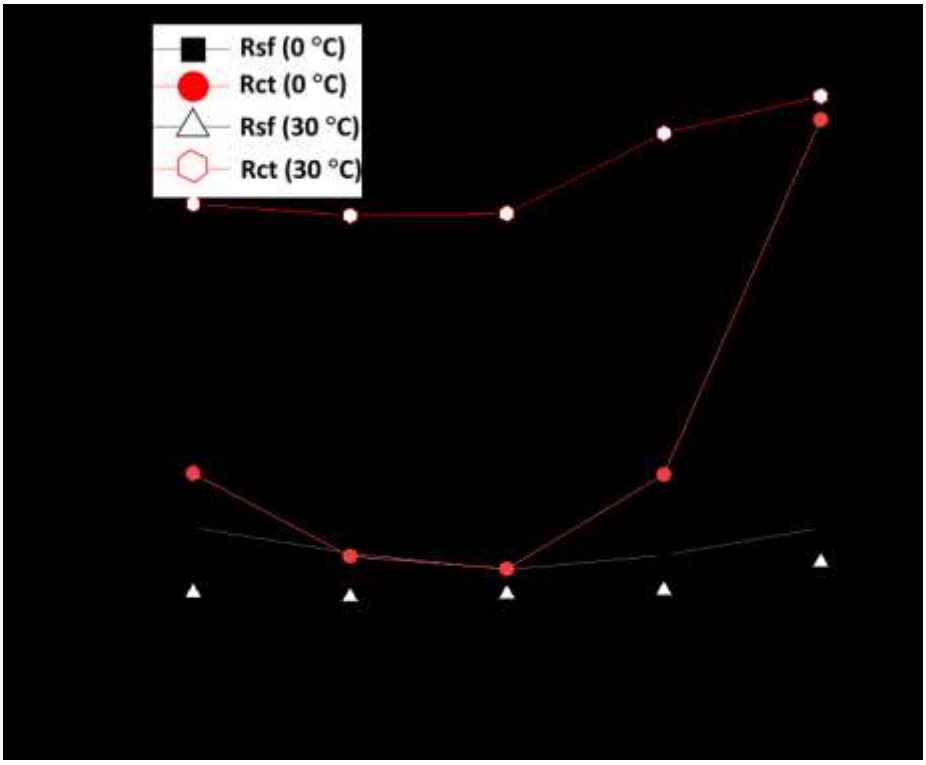

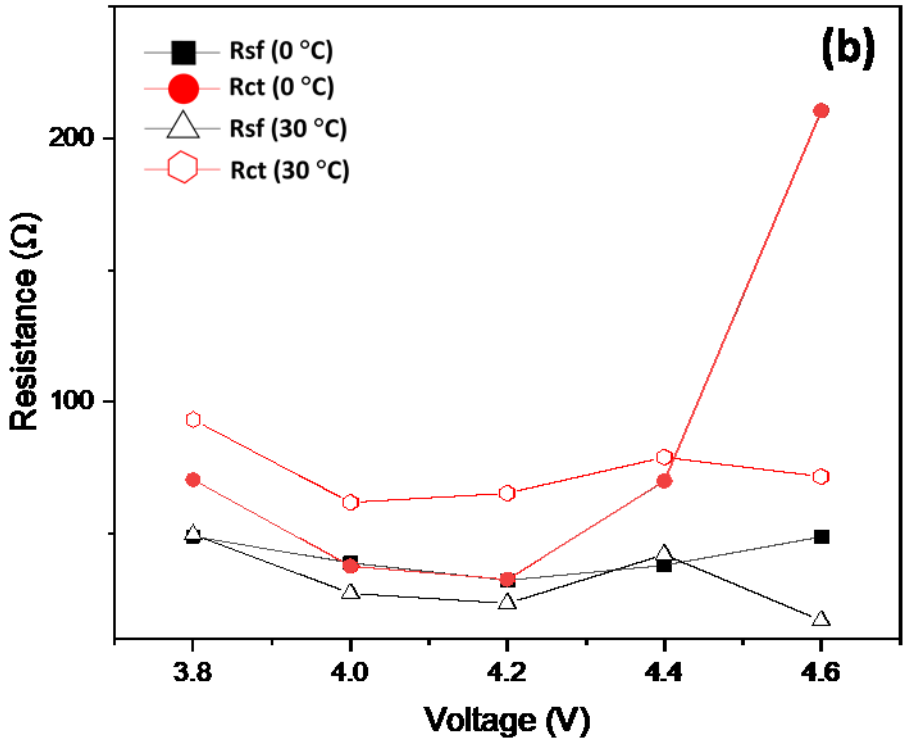

Figure 6a and **b**. Surface film (R_{sf}) and charge-transfer (R_{ct}) resistances calculated from impedance spectra measured at 30 °C from Li_2MnO_3 electrodes initially activated at 0 °C and 30 °C, respectively, as presented in **Figure 3b** for initial 7 cycles and subsequent cycles at 30 °C. The corresponding points of impedance measurements are marked with green stars in **Figure 3b.** Typical impedance spectra (Nyquist plots) of these electrodes measured at 30 °C at 4.4 V upon charging are displayed in **Figure S5**.

The continuous "activation" of the Li_2MnO_3 phase at 0 °C occurring upon charging to 4.7 V, at potentials of 4.50 – 4.55 V was supported by the results of GITT measurements in **Figure S6**. They confirm that only at 0 °C during the 1st charging process of Li_2MnO_3, the variation with time

of the transient electrode potential exhibits short plateau-like regions at 4.6 V followed by an extended plateau similarly to that in **Figure 2a.** Thus, we consider activation of Li_2MnO_3 electrodes at 0 °C as a step-by-step process that have not been detected in the initial cycles at the higher temperatures of 30 °C and 45 °C. A few questions, therefore, can be addressed, like: What is a possible impact of this step-by-step activation during several initial cycles at 0 °C on the subsequent electrode cycling at this temperature and at the higher temperatures? What is its effect on the capacity fading, evolution of the voltage hysteresis and electrode impedance? From the typical plot of the discharge capacity delivered by Li_2MnO_3 electrode activated at 0 °C and subsequently cycled at this temperature **(Figure 3a)**, it is clearly seen that after the activation cycles, the capacity increases smoothly reaching the maximal values of ~25 - 30 mAh/g. In contrast, much higher, by 3 - 4 times capacity can be obtained when Li_2MnO_3 is activated at low temperature of 0 °C and cycled then at the *higher temperatures* of 30 °C or 45 °C, as demonstrated by the cycling profiles (curves **A**) in **Figure 3b** and **c**, respectively. These results demonstrate that only when a few initial cycles were performed at a low temperature, providing step-by-step activation, the capacity increased substantially, its fading was less and the voltage hysteresis was considerably mitigated and stabilized upon cycling at the higher temperature (45 °C) as demonstrated in **Figure 3d.** We emphasize these findings are in line with those established by us, for the first time [34], that activation of Li and Mn-rich cathodes $0.35Li_2MnO_3{\cdot}Li[Mn_{0.45}Ni_{0.35}Co_{0.20}]O_2$ at low temperature resulted in an increased discharge capacity, decreased average charge voltage and the voltage hysteresis. As we noted in that paper, the results demonstrated by low temperature activation ("low-T activation") of the above cathodes were similar to those shown by other groups using potential window opening or step-wise

increasing anodic potential limits [8,37,68–70]. For instance, increased discharge capacity and decreased fading were observed by Sato et al. [70] and Ohsawa et al.[71], when the cells with $Li[Ni_{0.17}Li_{0.2}Co_{0.07}Mn_{0.56}]O_2$ cathodes were cycled through step-wise pre-cycling treatment, which included increasing the upper potential limit by 0.1 V from 4.5 V every two cycles to 4.8 V. This pre-cycling treatment means reaching and traversing for several times the voltage plateau, at which the Li-ions are extracted and the oxygen is released from the material. Dahn et al. [72] also came to a conclusion that many-step stepwise traverse of the oxygen-release plateau resulted in higher cycling capacities of Li and Mn-rich $Li[Li_{1/5}Ni_{1/5}Mn_{3/5}]O_2$ cathodes in Li-cells, compared to one-step oxygen release. By analyzing the literature data and the results obtained in the present work for Li_2MnO_3 electrodes activated at 0 °C, we assume that this "low-T activation" provides many-step stepwise traversing of the voltage plateau at >4.5 V during several cycles (from 2^{nd} to 5^{th}), **Figure 2a.** These short plateau-like portions were developed in a step-wise manner from the same cycling procedure upon charging Li_2MnO_3 to 4.7 V. The effect of the "low-T activation" is that the capacity of Li_2MnO_3 electrodes increases and level-offs upon further cycling at 30 °C in contrast to those activated in one-step at 30 °C and cycled at this temperature (**Figure 3b**, curves A and B, respectively). Stepwise activation at 0 °C also pronouncedly affects the further cycling of Li_2MnO_3 at 45 °C resulted in a stabilized performance after "low-T activation" as reflected by higher capacity retention and much lower and stabilized the voltage hysteresis, **Figure 3c** and **d**, respectively. These findings are crucially important since capacity fading and large voltage hysteresis are among the main problems to be resolved for Li and Mn-rich cathode materials in advanced LIBs [2,4,5]. Importantly to note that the effect of the "low-T activation" at 0 °C of Li_2MnO_3 discussed above confirms the hypothesized mechanism behind the improved

electrochemical behavior of $0.35Li_2MnO_3{\cdot}Li[Mn_{0.45}Ni_{0.35}Co_{0.20}]O_2$ materials activated at 0 °C, in our earlier work [34]. This mechanism suggested gradual step-wise activation of these electrodes at 0 °C allowing slower structural activation/reorganization of the Li_2MnO_3 component. This, in turn results in a greater degree of the TM-layer accessible for the Li^+ ions extraction/re-insertion and a smaller amount of the surface oxygen released. Indeed, as it was confirmed by our OEMS and XPS studies of Li_2MnO_3 electrodes activated at 0 °C, the amounts of O_2 evolved and per-oxo species formed were lower compared to those at 30 °C (**Figures 4** and **5,** respectively). Below, we present the results of some structural studies of Li_2MnO_3 electrodes initially activated at 0 °C and 30 °C.

3.3 Structural aspects of the initial cycling of Li_2MnO_3 electrodes at 0 °C and 30 °C

It is evident from the voltage profiles of Li_2MnO_3 electrodes initially cycled at 0 °C, 30 °C, and 45 °C (**Figure 2a, b and c**) that electrochemical activities were developed at around 3 V. We suggest these electrochemical processes reflect the formation of spinel or spinel-like phases as a result of the layered-to-spinel transformation typical for $Li(TM)O_2$ cathode materials during charge-discharge cycling [21,28,42]. **Figure 6** compares XRD patterns of uncycled (pristine) Li_2MnO_3 electrode and those initially charged to 4.7 V and discharged at 2.0 V at 0 °C and 30 °C, respectively.

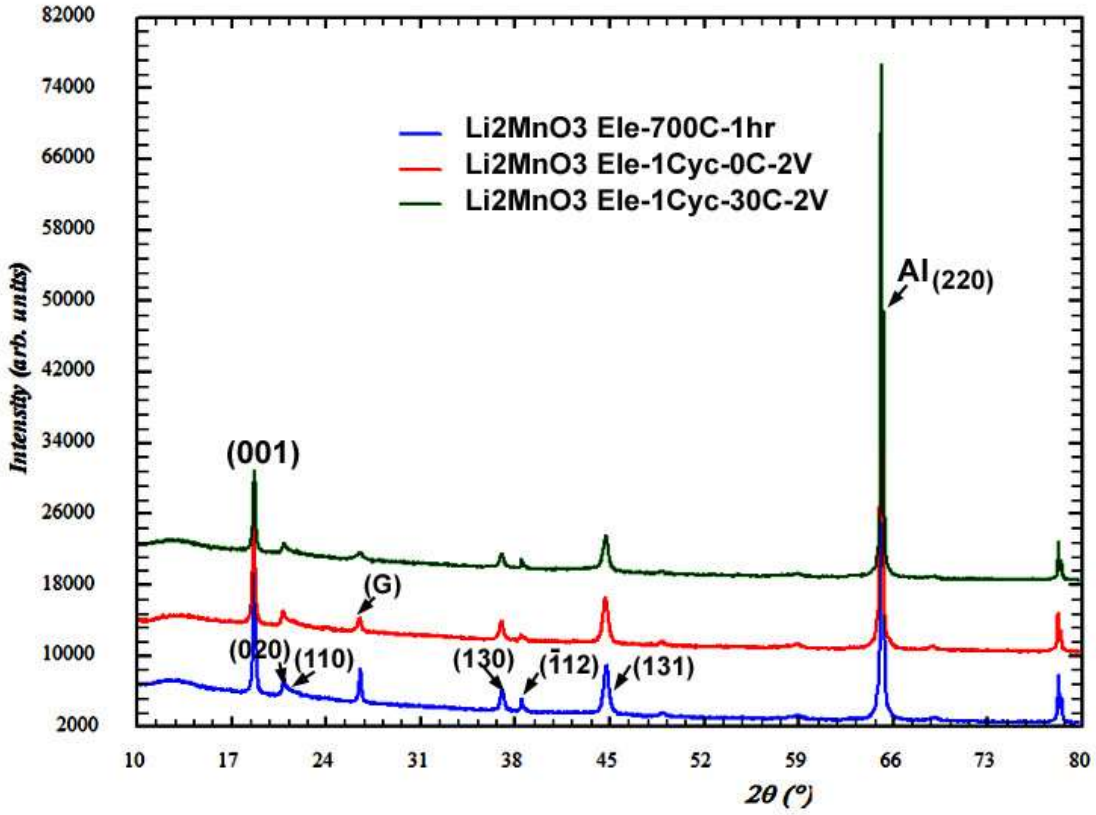

Figure 6. Comparison of XRD patterns recorded from Li_2MnO_3 electrodes on the Al-foil current collectors. Label G is related to a graphite peak, the peak at 2ϑ=65.1° is associated with (220) reflection from Al-foil. Blue, red and green profiles correspond, respectively, to as-prepared (annealed) powder and to electrodes subjected to the first charge-discharge cycle at 0 °C and 30 °C.

As it follows from **Table S1**, the unit cell parameters of cycled Li_2MnO_3 only slightly changed comparing to the pristine electrode. However, although the XRD patterns recorded from the cycled electrodes did not show any new peaks in addition to the peaks of the monoclinic phase, the TEM examinations, nevertheless, revealed that the tetragonal spinel $Li_2Mn_2O_4$ described by space group *I4amd* [73], is formed in electrodes even during the first charge/discharge cycle, both at 0

°C and at 30 °C. The cell parameters of $Li_2Mn_2O_4$ were calculated as follows: a=17.540 Å and c=8.205 Å. The corresponding TEM micrographs taken from samples subjected to the first cycle at 0 °C and at 30 °C are shown, respectively, in **Figure 7a** and **b.** The inserts in these figures represent the convergent-beam electron diffraction (CBED) patterns, which were taken from the grains indicated by arrows, with bottom inserts corresponding to the main monoclinic Li_2MnO_3 phase and upper inserts containing patterns indexed in terms of the tetragonal spinel $Li_2Mn_2O_4$. The upper insert in **Figure 7b** also contains an additional reflection system associated with the monoclinic phase (m). High-resolution image in **Figure S7** is an additional illustration of the presence of tetragonal spinel in the Li_2MnO_3 electrode after the first charge-discharge cycle. This image was taken from grain related to the upper insert in **Figure 7a.** As expected, the corresponding Fourier transform was indexed to the tetragonal spinel $Li_2Mn_2O_4$ in full accordance with the CBED pattern recorded from this grain.

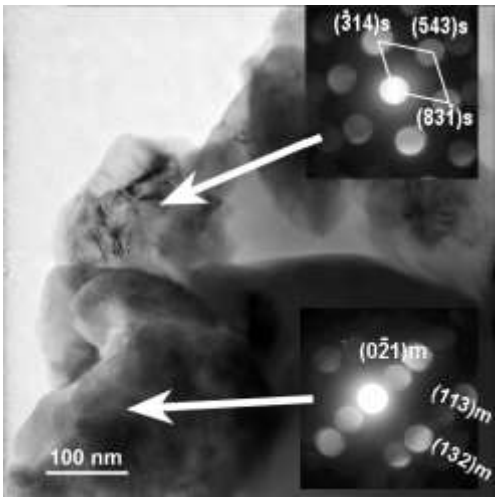

Figure 7a. TEM micrograph of Li_2MnO_3 electrode after the first charge/discharge cycle at 0 °C. The inserts show CBED patterns, which were taken from grains indicated by arrows. The pattern

in the bottom insert is indexed on the basis of the monoclinic Li_2MnO_3 phase (m), and the pattern in the upper insert demonstrates the presence of the tetragonal spinel $Li_2Mn_2O_4$ (s).

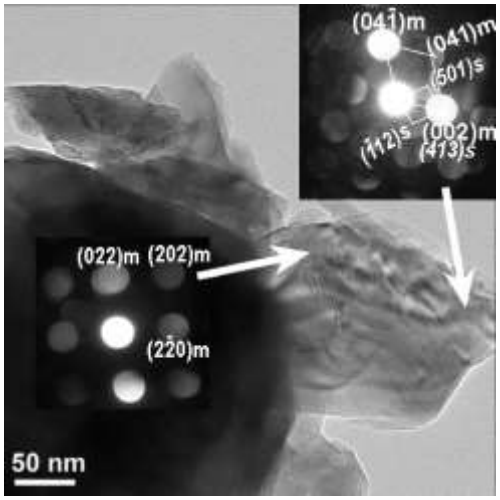

Figure 7b. TEM micrograph of Li_2MnO_3 electrode after the first charge/discharge cycle at 30 °C. The inserts show CBED patterns taken from grains indicated by arrows. The bottom pattern is indexed to the monoclinic Li_2MnO_3 phase (m), and the pattern in the upper insert contains two systems of reflections related to the monoclinic phase (m) and to the tetragonal spinel (s).

The results of the electron-diffraction studies demonstrating the formation of the spinel phase after the first cycle were supported by Raman spectroscopy measurements. Comparing the data in **Figure 8,** exhibits a typical Raman spectrum of pristine Li_2MnO_3 (uncycled) electrode with several well-resolved peaks (bands) located at 603, 560, 428, 409, 369, 305, and 246 cm^{-1}, in agreement with the literature reports on the monoclinic Li_2MnO_3 phase [59]. However, the Raman responses of electrodes subjected to the first cycle show some changes, namely a decreased intensity of the main peak at 603 cm^{-1}, its asymmetry and broadening related to a cationic disorder and increasing the amount of stacking faults [74].

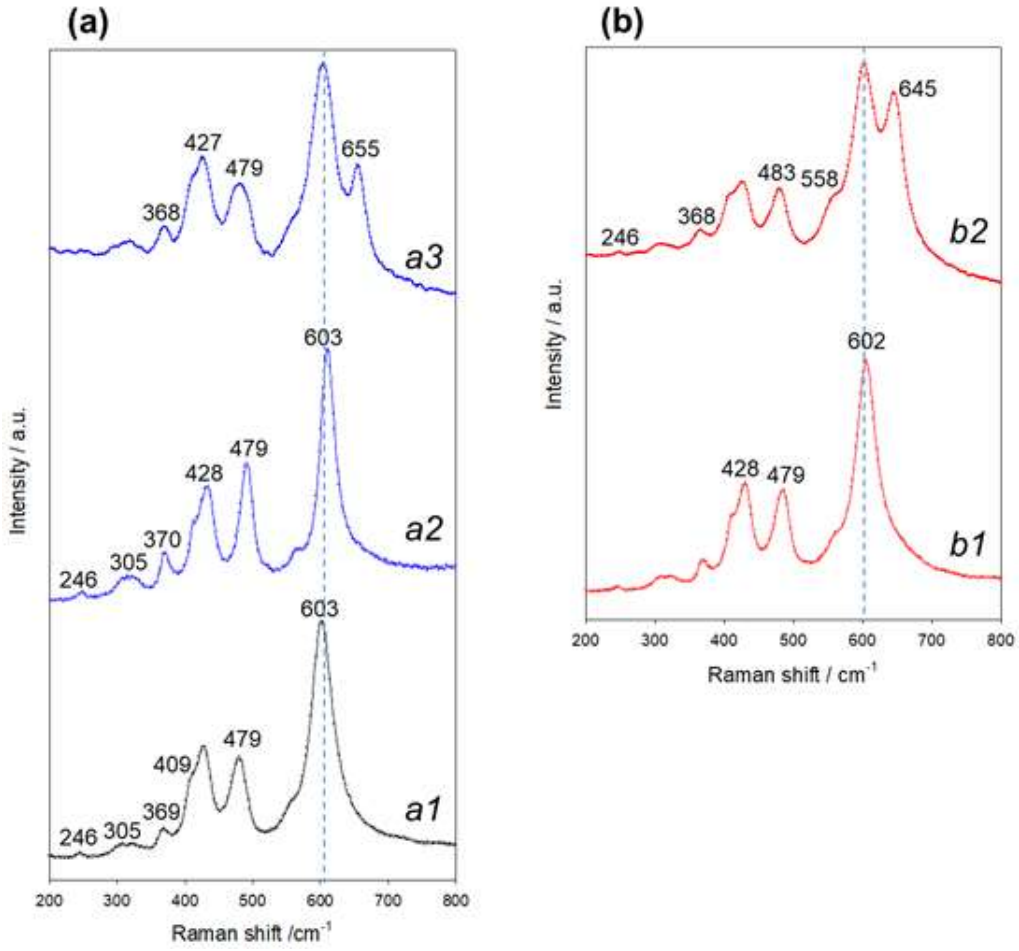

Figure 8 (***a***) Typical Raman spectra of pristine (uncycled) Li_2MnO_3 electrode (*a1*) and of a similar electrode after the 1st charge-discharge cycle at 0 °C measured at arbitrary locations (*a2*) and (*a3*); (***b***) spectra related to Li_2MnO_3 electrode after the 1st charge-discharge cycle at 30 °C measured at arbitrary locations (*b1*) and (*b2*).

We suggest that at anodic potentials > 4.5 V, the Li^+-ions can be further extracted from $LiMn_2O_4$ phase formed (due to the layered-to-spinel transition as demonstrated by electron diffraction studies in **Figures 7a** and **b**), providing emerging of new Raman bands at wavenumbers ~655 and

645 cm^{-1} in the spectra of Li_2MnO_3 electrodes cycled at 0 °C and 30 °C, respectively [75]. Upon the discharging process, Li^+ can be inserted into cubic spinel to form the tetragonal phase according to the following reaction:

$$LiMn_2O_4 + e^- + Li^+ \rightarrow Li_2Mn_2O_4. \quad (3)$$

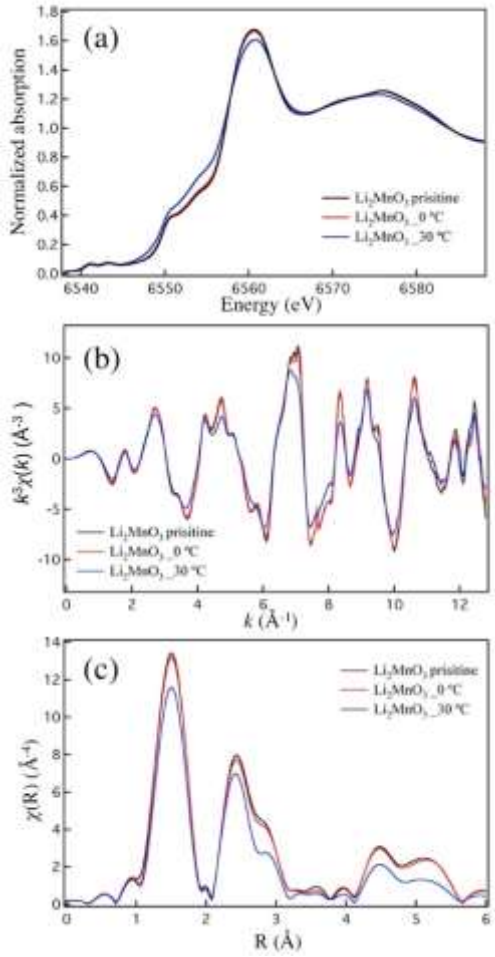

Figure 9. **(a)** Normalized Mn K-edge XANES spectra of Li_2MnO_3 samples: pristine powder and electrodes after the 1st cycle (charge to 4.7 V, discharge to 2.0 V) at 0 °C and 30 °C, as indicated. The voltage profiles of these electrodes are shown in **Figure 2a** and **b**, respectively. **(b)** k^3-weighted EXAFS $\chi(k)$ of Li_2MnO_3 samples: pristine powder and electrodes after the 1st cycle

(charge to 4.7 V, discharge to 2.0 V) at 0 °C and 30 °C, as indicated. The voltage profiles of these electrodes are shown in **Figure 2a** and **b**, respectively. **(c)** Fourier Transform magnitude of k^3-weighted EXAFS data ($|\chi(R)|$) of Li_2MnO_3 samples (k-range: 2.5-11 $Å^{-1}$; R_{bkg}:1.25 Å) shown in **Figure 2a** and **2b**.

An important piece of information on structural bulk and surface changes of Li_2MnO_3 electrodes subjected to initial charge-discharge cycles at 0 °C and 30 °C was obtained from EXAFS-XANES and high-resolution XPS studies. As seen in **Figure 9a**, the XANES data of the Li_2MnO_3 electrode cycled at 0 °C is almost identical to the as-prepared pristine material, which indicates the same oxidation state of Mn in these samples. Note that along with Mn^{4+}, some Mn^{3+} ions may also be present in the disordered surface layer of Li_2MnO_3 electrodes subjected to charge-discharge cycle. This is in accordance of analysis of magnetic characteristics of these electrodes at various states-of-charge as discussed in ref. [76]. In addition, one should take into account that Mn^{3+} containing species ($LiMnO_2$) can be formed upon oxygen release from the surface of Li_2MnO_3. Moreover, as it was shown in a recent work [77], based on calculation of Bader charges and magnetic moments, Mn oxidation state in HE-NCM can be reduced in the presence of per-oxo like $(O_2)^{2-}$ as a result of anionic charge over-compensation. The EXAFS data of Li_2MnO_3 cycled at 0 °C and 30 °C (**Figures 9b** and **c**, respectively) have similar features as the as-prepared pristine Li_2MnO_3. The major change in the electrode cycled at 30 °C is observed as the reduced amplitude in EXAFS data probably because of the structural disorder near the Mn sites. From fitting results (**Table S3** and **Figure S8**) of the EXAFS data, we conclude on an increase of the obtained Debye-Waller factors for Mn-O1 and Mn-Mn paths in Li_2MnO_3 sample cycled at 30 °C, compared with the as-prepared material and the one cycled at 0 °C. Such change in the Debye-Waller factors is very likely due to

the structural disorder near the Mn sites, which may be the main reason for the reduction of the amplitude of Mn-O1 and Mn-Mn peaks in Li_2MnO_3 electrode after charge-discharge at 30 °C.

High-resolution XPS data of the above samples also demonstrates that in Li_2MnO_3 electrodes subjected to initial cycling at 0 °C and 30 °C, some surface species are formed with the Mn-oxidation states of 3+ and 2+, respectively. This is evident from comparing XPS spectra of manganese. The Mn 2p structure of cycled samples (**Figure S9a**) is slightly shifted to lower energy and highly broaden at its lower-energy-side pointing to a possibility for the additional phases to be formed with the Mn valence lower than 4+ in pristine (uncycled) Li_2MnO_3. This is indeed confirmed by the measured Mn 3s structure that demonstrates the peak splitting (Δ, eV) higher than that of Li_2MnO_3, as illustrated in **Figure S9b**. For the pristine sample Δ~4.50 eV, whereas in initially cycled Li_2MnO_3 at 0 °C and 30 °C, the peak splitting values were estimated from XPS spectra as Δ~5.60 and Δ~6.30 eV, respectively that correspond to the Mn^{3+} and Mn^{2+} species formed on the surface of Li_2MnO_3 particles.

Conclusions

We established in this work that initial (activation) cycling of Li_2MnO_3 electrodes performed at 0 °C, results in increased discharge capacity, higher capacity retention, decreased and stabilized the voltage hysteresis upon subsequent cycling of these electrodes at the *higher temperatures* of 30 °C or 45 °C. This is due to the fact that at 0 °C, Li_2MnO_3 electrodes undergo step-by-step activation, providing a few-steps stepwise traversing of the voltage plateau at >4.5 V during several initial cycles. Importantly that activation cycling at 30 °C or 45 °C are characterized by the voltage plateaus at 4.60 and 4.55 V, respectively that were developed only in the first charging

process of Li_2MnO_3 electrodes. In contrary to 0 °C activation, this leads to considerable capacity fade and substantially increased the voltage hysteresis in further cycling. These findings are in accordance with those established by us previously [34], that activation at 0 °C of $0.35Li_2MnO_3{\cdot}Li[Mn_{0.45}Ni_{0.35}Co_{0.20}]O_2$ materials comprising Li_2MnO_3 as the main component responsible for excess capacity of these electrode, resulted in an increased discharge capacity, decreased average charge voltage and the voltage hysteresis. We conclude that the irreversible capacity loss of Li_2MnO_3 electrodes was the lowest at 0 °C, and the amount of per-oxo like species formed and the oxygen, H_2 and CO_2 released were also lower (compared to that at 30 °C and 45 °C), implying thus less interfacial side reactions and formation of an improved interface at 0 °C. Much lower the charge-transfer resistance of these electrodes calculated from impedance spectra measured upon charging to 4.7 V, also supports this conclusion. We furthermore conclude that Li_2MnO_3 preserved its bulk structure upon activation cycles at 0 °C and 30 °C with only some structural disorder near the Mn-sites (at 30 °C) and partial transformation (at the particle's surface) from the layered-type ordering to a tetragonal spinel $Li_2Mn_2O_4$ phase, typical for these systems.

We believe that the present work on initial (activation) cycling of Li_2MnO_3 at 0 °C resulting in improved stabilized behavior at higher temperatures, will stimulate further intensive research of Li and Mn-rich oxide materials for advanced LIBs.

Supplementary Materials: The following are available online at *www.mdpi.com/xxx/s1*,

Figure S1: Scanning Electron Microscopy image of the as-prepared Li_2MnO_3 annealed consequently at 400^0 and 700^0C for 1 h at each temperature, under air. **Figure S2**: XRD pattern collected from the as-prepared Li_2MnO_3 powder, which was annealed consequently at 400^0 and

700^{0}C for 1 h at each temperature, under air. **Figure S3:** High-resolution image taken from the particle indicated by the arrow in Figure 1. **Figure S4:** Differential capacity dQ/dV profiles of Li_2MnO_3 electrodes measured during several initial cycles at 0^{0}C (a), 30^{0}C (b), and 45^{0}C (c) as shown in Figure 3.

Table S1. Cell parameters of Li_2MnO_3 materials calculated from the corresponding XRD patterns.

Table S2. Results of XPS measurements of the lattice oxygen in Li_2MnO_3, per-oxo like and other components as calculated by fitting of the corresponding O 1s spectra measured from pristine (uncycled) Li_2MnO_3 electrode and those after initial activation cycles at 0^0 and 30^{0}C.

Table S3. Best fit results for the structural parameters obtained by analysis of the Mn K-edge EXAFS data of Li_2MnO_3 samples: pristine powder and electrodes after the 1st cycle (charge to 4.7 V, discharge to 2.0 V) at 0ºC and 30ºC.

Author Contributions: Conceptualization, B.M. and F.A.S.; methodology, E.E., B.M., F.A.S., A.F., J.L.; validation, F.A.S., M.T., L.B., A.F., J.L., R.; formal analysis, T.P., Y.T., R., M.N.; investigation, F.A.S., A.F., J.L., R.; data curation, B.M., M.T., A.F.; writing—original draft preparation, M.T., A.F., J.G., B.M.; writing—review and editing, B.M., D.A., Y.T.; visualization, J.L., M.T., T.P.; supervision, D.A.; project administration, D.A. All authors have read and agreed to the published version of the manuscript.

Acknowledgements:

A part of the work discussed herein is funded by the Israeli Prime Minister's Office and by the Israeli Committee for Higher Education within the framework of the INREP project. B.M. thanks Mr. Ronen Y. Tirrer from Electronics Unit, Bar-Ilan University for technical support and valuable suggestions. A.I.F. acknowledges support from the U. S. National Science Foundation Grant

number DMR-1911592. BL2-2 beamline operations were supported in part by the Synchrotron Catalysis Consortium (U.S. DOE, Office of Basic Energy Sciences, Grant No. DE-SC0012335).

References:

1. Thackeray, M.M.; Johnson, C.S.; Vaughey, J.T.; LiCurrent address: eVionyx Inc., Ha, N.; Hackney, S.A. Advances in manganese-oxide 'composite' electrodes for lithium-ion batteries. *J. Mater. Chem.* **2005**, *15*, 2257.

2. Nayak, P.K.; Erickson, E.M.; Schipper, F.; Penki, T.R.; Munichandraiah, N.; Adelhelm, P.; Sclar, H.; Amalraj, F.; Markovsky, B.; Aurbach, D. Review on Challenges and Recent Advances in the Electrochemical Performance of High Capacity Li- and Mn-Rich Cathode Materials for Li-Ion Batteries. *Adv. Energy Mater.* **2018**, *8*, 1702397.

3. Amalraj, F.; Talianker, M.; Markovsky, B.; Sharon, D.; Burlaka, L.; Shafir, G.; Zinigrad, E.; Haik, O.; Aurbach, D.; Lampert, J.; et al. Study of the Lithium-Rich Integrated Compound xLi 2 MnO 3 ·(1-x)LiMO 2 (x around 0.5; M = Mn, Ni, Co; 2:2:1) and Its Electrochemical Activity as Positive Electrode in Lithium Cells. *J. Electrochem. Soc.* **2013**, *160*, A324–A337.

4. Erickson, E.M.; Schipper, F.; Penki, T.R.; Shin, J.-Y.; Erk, C.; Chesneau, F.-F.; Markovsky, B.; Aurbach, D. Review—Recent Advances and Remaining Challenges for Lithium Ion Battery Cathodes. *J. Electrochem. Soc.* **2017**, *164*, A6341–A6348.

5. Zheng, J.; Myeong, S.; Cho, W.; Yan, P.; Xiao, J.; Wang, C.; Cho, J.; Zhang, J. Li- and Mn-Rich Cathode Materials: Challenges to Commercialization. *Adv. Energy Mater.* **2017**,

7, 1601284.

6. Kleiner, K.; Strehle, B.; Baker, A.R.; Day, S.J.; Tang, C.C.; Buchberger, I.; Chesneau, F.-F.; Gasteiger, H.A.; Piana, M. Origin of High Capacity and Poor Cycling Stability of Li-Rich Layered Oxides: A Long-Duration in Situ Synchrotron Powder Diffraction Study. *Chem. Mater.* **2018**, *30*, 3656–3667.

7. Jung, R.; Metzger, M.; Maglia, F.; Stinner, C.; Gasteiger, H.A. Oxygen Release and Its Effect on the Cycling Stability of LiNi x Mn y Co z O 2 (NMC) Cathode Materials for Li-Ion Batteries. *J. Electrochem. Soc.* **2017**, *164*, A1361–A1377.

8. Croy, J.R.; Gallagher, K.G.; Balasubramanian, M.; Long, B.R.; Thackeray, M.M. Quantifying Hysteresis and Voltage Fade in xLi 2 MnO 3 ● (1-x)LiMn 0.5 Ni 0.5 O 2 Electrodes as a Function of Li 2 MnO 3 Content. *J. Electrochem. Soc.* **2014**, *161*, A318–A325.

9. Sathiya, M.; Abakumov, A.M.; Foix, D.; Rousse, G.; Ramesha, K.; Saubanère, M.; Doublet, M.L.; Vezin, H.; Laisa, C.P.; Prakash, A.S.; et al. Origin of voltage decay in high-capacity layered oxide electrodes. *Nat. Mater.* **2015**, *14*, 230–238.

10. Hu, E.; Lyu, Y.; Xin, H.L.; Liu, J.; Han, L.; Bak, S.-M.; Bai, J.; Yu, X.; Li, H.; Yang, X.-Q. Explore the Effects of Microstructural Defects on Voltage Fade of Li- and Mn-Rich Cathodes. *Nano Lett.* **2016**, *16*, 5999–6007.

11. Croy, J.R.; Kim, D.; Balasubramanian, M.; Gallagher, K.; Kang, S.-H.; Thackeray, M.M. Countering the Voltage Decay in High Capacity xLi 2 MnO 3 •(1–x)LiMO 2 Electrodes (M=Mn, Ni, Co) for Li + -Ion Batteries. *J. Electrochem. Soc.* **2012**, *159*, A781–A790.

12. Yu, X.; Lyu, Y.; Gu, L.; Wu, H.; Bak, S.-M.; Zhou, Y.; Amine, K.; Ehrlich, S.N.; Li, H.; Nam, K.-W.; et al. Understanding the Rate Capability of High-Energy-Density Li-Rich Layered Li 1.2 Ni 0.15 Co 0.1 Mn 0.55 O 2 Cathode Materials. *Adv. Energy Mater.* **2014**, *4*, 1300950.

13. Lin, F.; Markus, I.M.; Nordlund, D.; Weng, T.-C.; Asta, M.D.; Xin, H.L.; Doeff, M.M. Surface reconstruction and chemical evolution of stoichiometric layered cathode materials for lithium-ion batteries. *Nat. Commun.* **2014**, *5*, 3529.

14. Gent, W.E.; Lim, K.; Liang, Y.; Li, Q.; Barnes, T.; Ahn, S.-J.; Stone, K.H.; McIntire, M.; Hong, J.; Song, J.H.; et al. Coupling between oxygen redox and cation migration explains unusual electrochemistry in lithium-rich layered oxides. *Nat. Commun.* **2017**, *8*, 2091.

15. Hu, E.; Yu, X.; Lin, R.; Bi, X.; Lu, J.; Bak, S.; Nam, K.-W.; Xin, H.L.; Jaye, C.; Fischer, D.A.; et al. Evolution of redox couples in Li- and Mn-rich cathode materials and mitigation of voltage fade by reducing oxygen release. *Nat. Energy* **2018**, *3*, 690–698.

16. Hy, S.; Felix, F.; Rick, J.; Su, W.-N.; Hwang, B.J. Direct In situ Observation of Li 2 O Evolution on Li-Rich High-Capacity Cathode Material, Li[Ni x Li (1–2 x)/3 Mn (2– x)/3]O 2 ($0 \leq x \leq 0.5$). *J. Am. Chem. Soc.* **2014**, *136*, 999–1007.

17. Xu, X.; Huo, H.; Jian, J.; Wang, L.; Zhu, H.; Xu, S.; He, X.; Yin, G.; Du, C.; Sun, X. Radially Oriented Single-Crystal Primary Nanosheets Enable Ultrahigh Rate and Cycling Properties of LiNi 0.8 Co 0.1 Mn 0.1 O 2 Cathode Material for Lithium-Ion Batteries. *Adv. Energy Mater.* **2019**, *9*, 1–9.

18. Singer, A.; Zhang, M.; Hy, S.; Cela, D.; Fang, C.; Wynn, T.A.; Qiu, B.; Xia, Y.; Liu, Z.; Ulvestad, A.; et al. Nucleation of dislocations and their dynamics in layered oxide cathode

materials during battery charging. *Nat. Energy* **2018**, *3*, 641–647.

19. Zhang, X.; Belharouak, I.; Li, L.; Lei, Y.; Elam, J.W.; Nie, A.; Chen, X.; Yassar, R.S.; Axelbaum, R.L. Structural and Electrochemical Study of Al 2 O 3 and TiO 2 Coated Li 1.2 Ni 0.13 Mn 0.54 Co 0.13 O 2 Cathode Material Using ALD. *Adv. Energy Mater.* **2013**, *3*, 1299–1307.

20. Zheng, J.; Yang, Z.; Wang, P.; Tang, L.; An, C.; He, Z. Multiple Linkage Modification of Lithium-Rich Layered Oxide Li 1.2 Mn 0.54 Ni 0.13 Co 0.13 O 2 for Lithium Ion Battery. *ACS Appl. Mater. Interfaces* **2018**, *10*, 31324–31329.

21. Amalraj, F.; Talianker, M.; Markovsky, B.; Burlaka, L.; Leifer, N.; Goobes, G.; Erickson, E.M.; Haik, O.; Grinblat, J.; Zinigrad, E.; et al. Studies of Li and Mn-Rich Li x [MnNiCo]O 2 Electrodes: Electrochemical Performance, Structure, and the Effect of the Aluminum Fluoride Coating. *J. Electrochem. Soc.* **2013**, *160*, A2220–A2233.

22. Nayak, P.K.; Grinblat, J.; Levi, M.; Levi, E.; Kim, S.; Choi, J.W.; Aurbach, D. Al Doping for Mitigating the Capacity Fading and Voltage Decay of Layered Li and Mn-Rich Cathodes for Li-Ion Batteries. *Adv. Energy Mater.* **2016**, *6*, 1502398.

23. Chen, G.; An, J.; Meng, Y.; Yuan, C.; Matthews, B.; Dou, F.; Shi, L.; Zhou, Y.; Song, P.; Wu, G.; et al. Cation and anion Co-doping synergy to improve structural stability of Li- and Mn-rich layered cathode materials for lithium-ion batteries. *Nano Energy* **2019**, *57*, 157–165.

24. Nayak, P.K.; Grinblat, J.; Levi, M.; Haik, O.; Levi, E.; Aurbach, D. Effect of Fe in suppressing the discharge voltage decay of high capacity Li-rich cathodes for Li-ion batteries. *J. Solid State Electrochem.* **2015**, *19*, 2781–2792.

25. Dong, X.; Xu, Y.; Xiong, L.; Sun, X.; Zhang, Z. Sodium substitution for partial lithium to significantly enhance the cycling stability of Li 2 MnO 3 cathode material. *J. Power Sources* **2013**, *243*, 78–87.

26. Dong, X.; Xu, Y.; Yan, S.; Mao, S.; Xiong, L.; Sun, X. Towards low-cost, high energy density Li 2 MnO 3 cathode materials. *J. Mater. Chem. A* **2015**, *3*, 670–679.

27. Breddemann, U.; Erickson, E.M.; Davis, V.; Schipper, F.; Ellwanger, M.; Daub, M.; Hoffmann, A.; Erk, C.; Markovsky, B.; Aurbach, D.; et al. Fluorination of Li-rich Lithium Ion Battery Cathode Materials by Fluorine Gas: Chemistry, Characterization, and Electrochemical Performance in Half Cells. *ChemElectroChem* **2019**, *3*, 3337–3349.

28. Erickson, E.M.; Sclar, H.; Schipper, F.; Liu, J.; Tian, R.; Ghanty, C.; Burstein, L.; Leifer, N.; Grinblat, J.; Talianker, M.; et al. High-Temperature Treatment of Li-Rich Cathode Materials with Ammonia: Improved Capacity and Mean Voltage Stability during Cycling. *Adv. Energy Mater.* **2017**, *7*, 1700708.

29. Shizuka, K.; Kiyohara, C.; Shima, K.; Takeda, Y. Effect of CO2 on layered Li1+zNi1−x−yCoxMyO2 (M=Al, Mn) cathode materials for lithium ion batteries. *J. Power Sources* **2007**, *166*, 233–238.

30. Sclar, H.; Sicklinger, J.; Erickson, E.M.; Maiti, S.; Grinblat, J.; Talianker, M.; Amalraj Susai, F.; Burstein, L.; Beyer, H.; Hartmann, L.; et al. Enhancement of Electrochemical Performance of Lithium and Manganese-Rich Cathode Materials via Thermal Treatment with SO 2. *J. Electrochem. Soc.* **2020**, *167*, 110563.

31. Johnson, C.S.; Kim, J.-S.; Lefief, C.; Li, N.; Vaughey, J.T.; Thackeray, M.M. The significance of the Li2MnO3 component in ‘composite’

xLi2MnO3·(1−x)LiMn0.5Ni0.5O2 electrodes. *Electrochem. commun.* **2004**, *6*, 1085–1091.

32. Rossouw, M.; Thackeray, M. Lithium manganese oxides from Li2MnO3 for rechargeable lithium battery applications. *Mater. Res. Bull.* **1991**, *26*, 463–473.

33. Maiti, S.; Sclar, H.; Rosy; Grinblat, J.; Talianker, M.; Burstein, L.; Noked, M.; Markovsky, B.; Aurbach, D. Modification of Li- and Mn-Rich Cathode Materials via Formation of the Rock-Salt and Spinel Surface Layers for Steady and High-Rate Electrochemical Performances. *ACS Appl. Mater. Interfaces* **2020**, *12*, 32698–32711.

34. Erickson, E.M.; Schipper, F.; Tian, R.; Shin, J.-Y.; Erk, C.; Chesneau, F.F.; Lampert, J.K.; Markovsky, B.; Aurbach, D. Enhanced capacity and lower mean charge voltage of Li-rich cathodes for lithium ion batteries resulting from low-temperature electrochemical activation. *RSC Adv.* **2017**, *7*, 7116–7121.

35. Thackeray, M.M.; Kang, S.-H.; Johnson, C.S.; Vaughey, J.T.; Benedek, R.; Hackney, S.A. Li2MnO3-stabilized LiMO2 (M = Mn, Ni, Co) electrodes for lithium-ion batteries. *J. Mater. Chem.* **2007**, *17*, 3112.

36. Shimoda, K.; Yazawa, K.; Matsunaga, T.; Murakami, M.; Yamanaka, K.; Ohta, T.; Matsubara, E.; Ogumi, Z.; Abe, T. Sequential delithiation behavior and structural rearrangement of a nanoscale composite-structured Li1.2Ni0.2Mn0.6O2 during charge–discharge cycles. *Sci. Rep.* **2020**, *10*, 10048.

37. Croy, J.R.; Gallagher, K.G.; Balasubramanian, M.; Chen, Z.; Ren, Y.; Kim, D.; Kang, S.-H.; Dees, D.W.; Thackeray, M.M. Examining Hysteresis in Composite x Li 2 MnO 3 ·(1–x)LiMO 2 Cathode Structures. *J. Phys. Chem. C* **2013**, *117*, 6525–6536.

38. Assat, G.; Iadecola, A.; Foix, D.; Dedryvère, R.; Tarascon, J.-M. Direct Quantification of Anionic Redox over Long Cycling of Li-Rich NMC via Hard X-ray Photoemission Spectroscopy. *ACS Energy Lett.* **2018**, *3*, 2721–2728.

39. Lu, Z.; Dahn, J.R. Understanding the Anomalous Capacity of Li/Li[Ni[sub x]Li[sub (1/3−2x/3)]Mn[sub (2/3−x/3)]]O[sub 2] Cells Using In Situ X-Ray Diffraction and Electrochemical Studies. *J. Electrochem. Soc.* **2002**, *149*, A815.

40. Yu, D.Y.W.; Yanagida, K.; Kato, Y.; Nakamura, H. Electrochemical Activities in Li[sub 2]MnO[sub 3]. *J. Electrochem. Soc.* **2009**, *156*, A417.

41. Phillips, P.J.; Bareño, J.; Li, Y.; Abraham, D.P.; Klie, R.F. On the Localized Nature of the Structural Transformations of Li 2 MnO 3 Following Electrochemical Cycling. *Adv. Energy Mater.* **2015**, *5*, 1501252.

42. Francis Amalraj, S.; Markovsky, B.; Sharon, D.; Talianker, M.; Zinigrad, E.; Persky, R.; Haik, O.; Grinblat, J.; Lampert, J.; Schulz-Dobrick, M.; et al. Study of the electrochemical behavior of the "inactive" Li2MnO3. *Electrochim. Acta* **2012**, *78*, 32–39.

43. Yu, H.; Ishikawa, R.; So, Y.-G.; Shibata, N.; Kudo, T.; Zhou, H.; Ikuhara, Y. Direct Atomic-Resolution Observation of Two Phases in the Li 1.2 Mn 0.567 Ni 0.166 Co 0.067 O 2 Cathode Material for Lithium-Ion Batteries. *Angew. Chemie Int. Ed.* **2013**, *52*, 5969–5973.

44. Xu, B.; Fell, C.R.; Chi, M.; Meng, Y.S. Identifying surface structural changes in layered Li-excess nickel manganese oxides in high voltage lithium ion batteries: A joint experimental and theoretical study. *Energy Environ. Sci.* **2011**, *4*, 2223.

45. Rana, J.; Stan, M.; Kloepsch, R.; Li, J.; Schumacher, G.; Welter, E.; Zizak, I.; Banhart, J.; Winter, M. Structural Changes in Li 2 MnO 3 Cathode Material for Li-Ion Batteries. *Adv. Energy Mater.* **2014**, *4*, 1300998.

46. Chen, H.; Islam, M.S. Lithium Extraction Mechanism in Li-Rich Li 2 MnO 3 Involving Oxygen Hole Formation and Dimerization. *Chem. Mater.* **2016**, *28*, 6656–6663.

47. Seo, D.H.; Lee, J.; Urban, A.; Malik, R.; Kang, S.; Ceder, G. The structural and chemical origin of the oxygen redox activity in layered and cation-disordered Li-excess cathode materials. *Nat. Chem.* **2016**, *8*, 692–697.

48. Cao, T.; Shi, C.; Zhao, N.; He, C.; Li, J.; Liu, E. Understanding the Electrochemical Properties of Li-Rich Cathode Materials from First-Principles Calculations. *J. Phys. Chem. C* **2015**, *119*, 28749–28756.

49. Lee, E.; Persson, K.A. Structural and Chemical Evolution of the Layered Li-Excess Li x MnO 3 as a Function of Li Content from First-Principles Calculations. *Adv. Energy Mater.* **2014**, *4*, 1400498.

50. Zhang, Z.; Zhao, S.; Wang, B.; Yu, H. Local Redox Reaction of High Valence Manganese in Li2MnO3-Based Lithium Battery Cathodes. *Cell Reports Phys. Sci.* **2020**, *1*, 100061.

51. Amalraj, S.F.; Sharon, D.; Talianker, M.; Julien, C.M.; Burlaka, L.; Lavi, R.; Zhecheva, E.; Markovsky, B.; Zinigrad, E.; Kovacheva, D.; et al. Study of the nanosized Li2MnO3: Electrochemical behavior, structure, magnetic properties, and vibrational modes. *Electrochim. Acta* **2013**, *97*, 259–270.

52. Hershkovitz, S.; Baltianski, S.; Tsur, Y. Electrochemical Impedance Analysis of SOFC

Cathode Reaction Using Evolutionary Programming. *Fuel Cells* **2012**, *12*, 77–85.

53. Oz, A.; Gelman, D.; Goren, E.; Shomrat, N.; Baltianski, S.; Tsur, Y. A novel approach for supercapacitors degradation characterization. *J. Power Sources* **2017**, *355*, 74–82.

54. Kalimuthu, V.S.; Attias, R.; Tsur, Y. Electrochemical impedance spectra of RuO2 during oxygen evolution reaction studied by the distribution function of relaxation times. *Electrochem. commun.* **2020**, *110*, 106641.

55. Kraus, W.; Nolze, G. POWDER CELL – a program for the representation and manipulation of crystal structures and calculation of the resulting X-ray powder patterns. *J. Appl. Crystallogr.* **1996**, *29*, 301–303.

56. Rodríguez-Carvajal, J. Recent advances in magnetic structure determination by neutron powder diffraction. *Phys. B Condens. Matter* **1993**, *192*, 55–69.

57. Gabrisch, H.; Yi, T.; Yazami, R. Transmission Electron Microscope Studies of LiNi[sub 1/3]Mn[sub 1/3]Co[sub 1/3]O[sub 2] before and after Long-Term Aging at 70°C. *Electrochem. Solid-State Lett.* **2008**, *11*, A119.

58. Ravel, B.; Newville, M. ATHENA , ARTEMIS , HEPHAESTUS : data analysis for X-ray absorption spectroscopy using IFEFFIT. *J. Synchrotron Radiat.* **2005**, *12*, 537–541.

59. Julien, C.M.; Massot, M. Lattice vibrations of materials for lithium rechargeable batteries III. Lithium manganese oxides. *Mater. Sci. Eng. B* **2003**, *100*, 69–78.

60. Strobel, P.; Lambert-Andron, B. Crystallographic and magnetic structure of Li2MnO3. *J. Solid State Chem.* **1988**, *75*, 90–98.

61. Ye, D.; Sun, C.; Chen, Y.; Ozawa, K.; Hulicova-jurcakova, D.; Zou, J. Ni-induced

stepwise capacity increase in Ni-poor Li- rich cathode materials for high performance lithium ion. **2015**, *8*, 808–820.

62. Strehle, B.; Kleiner, K.; Jung, R.; Chesneau, F.; Mendez, M.; Gasteiger, H.A.; Piana, M. The Role of Oxygen Release from Li- and Mn-Rich Layered Oxides during the First Cycles Investigated by On-Line Electrochemical Mass Spectrometry. *J. Electrochem. Soc.* **2017**, *164*, A400–A406.

63. Teufl, T.; Strehle, B.; Müller, P.; Gasteiger, H.A.; Mendez, M.A. Oxygen Release and Surface Degradation of Li- and Mn-Rich Layered Oxides in Variation of the Li 2 MnO 3 Content. *J. Electrochem. Soc.* **2018**, *165*, A2718–A2731.

64. Muhammad, S.; Kim, H.; Kim, Y.; Kim, D.; Song, J.H.; Yoon, J.; Park, J.-H.; Ahn, S.-J.; Kang, S.-H.; Thackeray, M.M.; et al. Evidence of reversible oxygen participation in anomalously high capacity Li- and Mn-rich cathodes for Li-ion batteries. *Nano Energy* **2016**, *21*, 172–184.

65. Saubanère, M.; McCalla, E.; Tarascon, J.-M.; Doublet, M.-L. The intriguing question of anionic redox in high-energy density cathodes for Li-ion batteries. *Energy Environ. Sci.* **2016**, *9*, 984–991.

66. Rozier, P.; Tarascon, J.M. Review—Li-Rich Layered Oxide Cathodes for Next-Generation Li-Ion Batteries: Chances and Challenges. *J. Electrochem. Soc.* **2015**, *162*, A2490–A2499.

67. Chen, Q.; Pei, Y.; Chen, H.; Song, Y.; Zhen, L.; Xu, C.-Y.; Xiao, P.; Henkelman, G. Highly reversible oxygen redox in layered compounds enabled by surface polyanions. *Nat. Commun.* **2020**, *11*, 3411.

68. Ohzuku, T.; Nagayama, M.; Tsuji, K.; Ariyoshi, K. High-capacity lithium insertion materials of lithium nickel manganese oxides for advanced lithium-ion batteries: toward rechargeable capacity more than 300 mA h g−1. *J. Mater. Chem.* **2011**, *21*, 10179.

69. WATANABE, A.; MATSUMOTO, F.; FUKUNISHI, M.; KOBAYASHI, G.; ITO, A.; HATANO, M.; OHSAWA, Y.; SATO, Y. Relationship between Electrochemical Pre-Treatment and Cycle Performance of a Li-Rich Solid-Solution Layered Li1^|^minus;^|^alpha;[Ni0.18Li0.20+^|^alpha;Co0.03Mn0.58]O2 Cathode for Li-Ion Secondary Batteries. *Electrochemistry* **2012**, *80*, 561–565.

70. Ito, A.; Li, D.; Ohsawa, Y.; Sato, Y. A new approach to improve the high-voltage cyclic performance of Li-rich layered cathode material by electrochemical pre-treatment. *J. Power Sources* **2008**, *183*, 344–346.

71. Ito, A.; Li, D.; Sato, Y.; Arao, M.; Watanabe, M.; Hatano, M.; Horie, H.; Ohsawa, Y. Cyclic deterioration and its improvement for Li-rich layered cathode material Li[Ni0.17Li0.2Co0.07Mn0.56]O2. *J. Power Sources* **2010**, *195*, 567–573.

72. van Bommel, A.; Krause, L.J.; Dahn, J.R. Investigation of the Irreversible Capacity Loss in the Lithium-Rich Oxide Li[Li1/5Ni1/5Mn3/5]O2. *J. Electrochem. Soc.* **2011**, *158*, A731.

73. Wills, A.S.; Raju, N.P.; Greedan, J.E. Low-Temperature Structure and Magnetic Properties of the Spinel LiMn 2 O 4 : A Frustrated Antiferromagnet and Cathode Material. *Chem. Mater.* **1999**, *11*, 1510–1518.

74. Nakashima, S.; Nakatake, Y.; Harima, H.; Katsuno, M.; Ohtani, N. Detection of stacking faults in 6H-SiC by Raman scattering. *Appl. Phys. Lett.* **2000**, *77*, 3612–3614.

75. Leifer, N.; Schipper, F.; Erickson, E.M.; Ghanty, C.; Talianker, M.; Grinblat, J.; Julien, C.M.; Markovsky, B.; Aurbach, D. Studies of Spinel-to-Layered Structural Transformations in LiMn 2 O 4 Electrodes Charged to High Voltages. *J. Phys. Chem. C* **2017**, *121*, 9120–9130.

76. Amalraj, S.F.; Burlaka, L.; Julien, C.M.; Mauger, A.; Kovacheva, D.; Talianker, M.; Markovsky, B.; Aurbach, D. Phase Transitions in Li2MnO3 Electrodes at Various States-of-Charge. *Electrochim. Acta* **2014**, *123*, 395–404.

77. Marusczyk, A.; Albina, J.-M.; Hammerschmidt, T.; Drautz, R.; Eckl, T.; Henkelman, G. Oxygen activity and peroxide formation as charge compensation mechanisms in Li 2 MnO 3. *J. Mater. Chem. A* **2017**, *5*, 15183–15190.